



The primary structural photoresponse of phytochrome proteins captured by a femtosecond X-ray laser

Elin Claesson^{1†}, Weixiao Yuan Wahlgren^{1†}, Heikki Takala^{2,3†}, Suraj Pandey⁴, Leticia Castillon¹, Valentyna Kuznetsova², Léocadie Henry¹, Matthijs Panman¹, Melissa Carrillo⁵, Joachim Kübel¹, Rahul Nanekar², Linnéa Isaksson¹, Amke Nimmrich¹, Andrea Cellini¹, Dmitry Morozov⁶, Michał Maj¹, Moona Kurttila², Robert Bosman¹, Eriko Nango^{7,8}, Rie Tanaka^{7,8}, Tomoyuki Tanaka^{7,8}, Luo Fangjia^{7,8}, So Iwata^{7,8}, Shigeki Owada^{8,9}, Keith Moffat¹⁰, Gerrit Groenhof⁶, Emina A Stojković⁵, Janne A Ihalainen², Marius Schmidt^{4*}, Sebastian Westenhoff^{1*}

¹Department of Chemistry and Molecular Biology, University of Gothenburg, Gothenburg, Sweden; ²Department of Biological and Environmental Science, Nanoscience Center, University of Jyvaskyla, Jyvaskyla, Finland; ³Department of Anatomy, Faculty of Medicine, University of Helsinki, Helsinki, Finland; ⁴Physics Department, University of Wisconsin-Milwaukee, Milwaukee, United States; ⁵Department of Biology, Northeastern Illinois University, Chicago, United States; ⁶Department of Chemistry, Nanoscience Center, University of Jyvaskyla, Jyvaskyla, Finland; ⁷Department of Cell Biology, Graduate School of Medicine, Kyoto University, Kyoto, Japan; ⁸RIKEN SPring-8 Center, Hyogo, Japan; ⁹Japan Synchrotron Radiation Research Institute, Hyogo, Japan; ¹⁰Department of Biochemistry and Molecular Biology and Institute for Biophysical Dynamics, University of Chicago, Chicago, United States

Abstract Phytochrome proteins control the growth, reproduction, and photosynthesis of plants, fungi, and bacteria. Light is detected by a bilin cofactor, but it remains elusive how this leads to activation of the protein through structural changes. We present serial femtosecond X-ray crystallographic data of the chromophore-binding domains of a bacterial phytochrome at delay times of 1 ps and 10 ps after photoexcitation. The data reveal a twist of the D-ring, which leads to partial detachment of the chromophore from the protein. Unexpectedly, the conserved so-called pyrrole water is photodissociated from the chromophore, concomitant with movement of the A-ring and a key signaling aspartate. The changes are wired together by ultrafast backbone and water movements around the chromophore, channeling them into signal transduction towards the output domains. We suggest that the observed collective changes are important for the phytochrome photoresponse, explaining the earliest steps of how plants, fungi and bacteria sense red light.

smarius@uwm.edu (MS); sebastian.westenhoff.2@gu.se (SW)

*For correspondence:

[†]These authors contributed equally to this work

Competing interests: The authors declare that no competing interests exist.

Funding: See page 14

Received: 11 November 2019 Accepted: 13 March 2020 Published: 31 March 2020

Reviewing editor: Werner Kühlbrandt, Max Planck Institute of Biophysics, Germany

© Copyright Claesson et al. This article is distributed under the terms of the Creative Commons Attribution License, which permits unrestricted use and redistribution provided that the original author and source are credited.

Introduction

Phytochrome photosensor proteins are crucial for the optimal development of all vegetation on Earth (*Butler et al., 1959*; *Gan et al., 2014*; *Quail et al., 1995*). Prototypical phytochromes can exist in two photochemical states with differential cellular signaling activity, called red light-absorbing (Pr) and far-red light-absorbing (Pfr) state (*Figure 1—figure supplement 1*). As a result, phytochromes



eLife digest Plants adapt to the availability of light throughout their lives because it regulates so many aspects of their growth and reproduction. To detect the level of light, plant cells use proteins called phytochromes, which are also found in some bacteria and fungi. Phytochrome proteins change shape when they are exposed to red light, and this change alters the behaviour of the cell. The red light is absorbed by a molecule known as chromophore, which is connected to a region of the phytochrome called the PHY-tongue. This region undergoes one of the key structural changes that occur when the phytochrome protein absorbs light, turning from a flat sheet into a helix.

Claesson, Wahlgren, Takala et al. studied the structure of a bacterial phytochrome protein almost immediately after shining a very brief flash of red light using a laser. The experiments revealed that the structure of the protein begins to change within a trillionth of a second: specifically, the chromophore twists, which disrupts its attachment to the protein, freeing the protein to change shape. Claesson, Wahlgren, Takala et al. note that this structure is likely a very short-lived intermediate state, which however triggers more changes in the overall shape change of the protein.

One feature of the rearrangement is the disappearance of a particular water molecule. This molecule can be found at the core of many different phytochrome structures and interacts with several parts of the chromophore and the phytochrome protein. It is unclear why the water molecule is lost, but given how quickly this happens after the red light is applied it is likely that this disappearance is an integral part of the reshaping process.

Together these events disrupt the interactions between the chromophore and the PHY-tongue, enabling the PHY-tongue to change shape and alter the structure of the phytochrome protein. Understanding and controlling this process could allow scientists to alter growth patterns in plants, such as crops or weeds.

can distinguish two colors of light, providing plants, fungi, and bacteria with primitive two-color vision. Light is detected by a bilin chromophore, which is covalently linked to the photosensory core of the protein (*Wagner et al., 2005*), comprising of PAS (Per/Arndt/Sim), GAF (cGMP phosphodiesterase/adenyl cyclase/FhlA) and PHY (phytochrome-specific) domains. Two propionate side chains additionally anchor the chromophore non-covalently to the protein (*Figure 1b*). The signaling sites of the phytochrome are found in its C- and N-terminal output domains, which vary between species. Important for the signaling is a stretch of amino acids in the PHY domain, called the PHY-tongue, which changes from a β -sheet in Pr into an α -helix in Pfr state (*Essen et al., 2008*; *Yang et al., 2008*; *Takala et al., 2014*; *Sanchez et al., 2019*) The chromophore connects to the PHY-tongue via a strictly conserved aspartatic acid, which is expected to play a crucial role in signal transduction.

Key to phytochrome function is the primary photoresponse on picosecond time scales. Here, light signals are translated into conformational changes. The changes arise in the electronically excited bilin, but must then be transduced to the surrounding protein residues. This prepares the protein for a formation of the first intermediate (Lumi-R for prototypical phytochromes), in which isomerization of the D-ring has likely occurred (*Rüdiger et al., 1983*; *Dasgupta et al., 2009*; *Yang et al., 2012*; *Rockwell et al., 2009*; *Ihalainen et al., 2018*). The mechanism that leads to the first intermediate is currently not well understood, because crystallographic observations of phytochromes directly after photoexcitation have not been available.

Results

To address this gap of knowledge, we recorded time-resolved serial femtosecond X-ray crystallographic (SFX) data of the PAS-GAF domains of the phytochrome from *Deinococcus radiodurans* ($DrBphP_{CBD}$) at 1 ps and 10 ps after femtosecond optical excitation. The experiments were performed in Japan, using the SPring-8 Angstrom Compact Free Electron Laser (SACLA) tuned to 7 KeV (*Tono et al., 2015*). For homogeneous excitation of the crystals, we photoexcited micrometer-sized crystals in a grease jet with a photon density of 1.7 mJ/mm² ($1/e^2$ measure, see Materials and methods) into the flank of the absorption peak at 640 nm (*Figure 1—figure supplement 1*). Taking into account the significant light scattering in the grease-buffer mixture (*Figure 1—figure 1—figure*



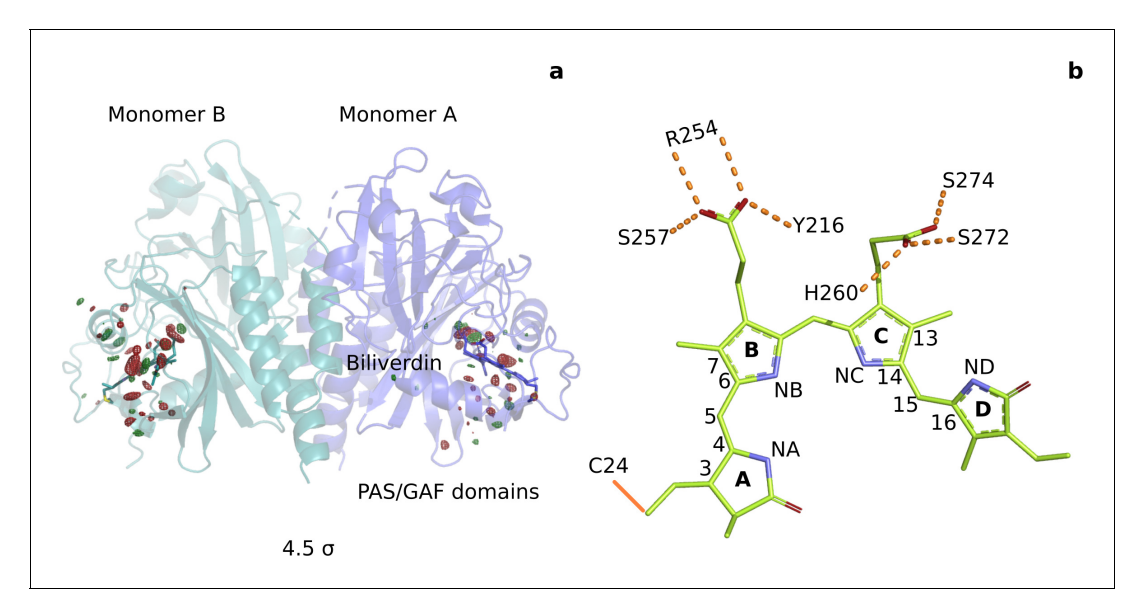


Figure 1. Photoinduced observed difference electron density features are focused on the chromophore binding pocket. (a) The observed difference electron density map at 1 ps is displayed together with the $DrBphP_{dark}$ structure. Red and green electron density peaks, contoured at $4.5 \, \sigma$, denote negative and positive densities, respectively. Monomer A is colored blue and monomer B is in aqua. (b) Schematic illustration of the biliverdin chromophore. The hydrogen-bonding networks between the propionate groups and the protein are marked with dashed lines. In DrBphP, the chromophore is covalently linked to a cysteine residue in the PAS domain (solid line).

The online version of this article includes the following figure supplement(s) for figure 1:

Figure supplement 1. The photocycle of *Deinococcus radiodurans* phytochrome (*Dr*BphP) and the spectral properties of its PAS-GAF fragment in the microcrystalline form.

Figure supplement 2. Microcrystals used for SFX data acquisition in SACLA.

Figure supplement 3. Unit cell parameters distribution of SFX data sets.

Figure supplement 4. Significant difference electron density features observed.

Figure supplement 5. Comparison of the observed difference electron density maps at 1 ps and 10 ps.

supplement 1), we estimate that the average number of photons per chromophore is 0.5–1 (see Materials and methods). We recorded the SFX data at 1 ps for several excitation fluences (*Figure 2*). Lowering the excitation density tenfold from 1.7 mJ/mm² photons to 0.2 mJ/mm² resulted in a joint reduction of all difference signals. Critical signals, like the twist of the D-ring and the photodissociation of the pyrrole water from the chromophore sustained when lowering the excitation densities, indicating that the signal arises predominately from one-photon excitation. The refined structure in dark (*Dr*BphP_{dark}), 2.07 Å resolution (*Table 1*), was very similar to our previous dark structure solved by SFX (5K5B, RMSD 0.646 Å and 0.610 Å for monomers A and B) (*Edlund et al., 2016*), but the present crystals contained two monomers in the asymmetric unit (*Figure 1a, Figure 1—figure supplement 2, Figure 1—figure supplement 3*). The refined 1 ps structure was solved to 2.21 Å (*Table 1*).

From the time-resolved data, we calculated Fourier difference electron density maps $(|F_o|^{light} - |F_o|^{dark})$, which report on the change of structure due to optical excitation (see Materials and methods). Briefly, the diffraction data for light and dark were scaled to each other and subtracted, assuming preservation of the phases (see Materials and methods for details). The map at 1 ps indicates many significant changes in difference electron density (*Figure 1a*) above the background level of 3.0 standard deviations (σ) (*Figure 1—figure supplement 4*). The changes cluster around the chromophore, with the strongest negative densities for the pyrrole water (monomer A: -8.2σ , B: -9.4σ , *Table 2*). The map at 10 ps contains similar significant features, but at weaker overall intensity (pyrrole water A: -5.0σ , B: -6.5σ) (*Figure 1—figure supplement 4* and *Figure 1—figure supplement 5*). We ascribe this to a lower population of the activated state at 10 ps compared to 1 ps. Monomer A has a lower signal strength than monomer B, but provided a clearer difference map around the chromophore. We refined a structural model (*Dr*BphP_{1ps}) using extrapolated



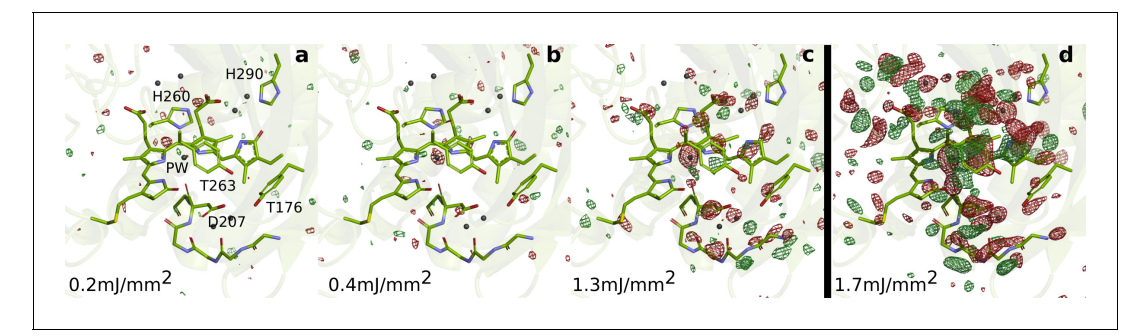


Figure 2. SFX data as a function of excitation fluence. The $DrBphP_{dark}$ structure (green) is shown together with the observed difference electron density, contoured at 3.5 σ, at 1 ps collected using (a) 0.2 mJ/mm², (b) 0.4 mJ/mm², (c) 1.3 mJ/mm², and (d) 1.7 mJ/mm². All spot sizes were computed assuming Gaussian line shapes with the $(1/e^2)$ convention. The data shown in panel A-C were collected at SACLA in May 2019, whereas the data shown in panel D was collected in October 2018. The same experimental setup was used in both occasions. The laser energy of the experiment in 2018 can be found in the Materials and methods section. The energies for the experiment in 2019 were 16 μJ, 42 μJ, and 106 μJ (panels A-C, respectively). During the experiment in 2019, the femtosecond laser beam was misaligned by 50 μm distance from the interaction spot between X-rays and jet in the direction of flow. The laser intensities were corrected for this displacement assuming a Gaussian line shape. The excitation fluence is similar to previous femtosecond time-resolved SFX experiments (**Nogly et al., 2018**; **Pande et al., 2016**; **Barends et al., 2015**; **Coquelle et al., 2018**); however, we found high scattering in the grease/buffer mixture (**Figure 1—figure supplement 1**). Since the crystallographic signals were reduced when lowering the excitation fluence and disappeared completely when reaching 1/10 of the maximum value, we conclude that the excitation fluence that actually reaches the crystals in the grease matrix is much lower than the incoming photon fluence and that the photoexcitation is in the single-photon regime.

structure factors (*Figure 3—figure supplement 1*; *Pande et al., 2016*). The refinement of the structure against the 1 ps data was successful using a photoexcitation density of 8%. However, we aborted our attempts to refine a structural model against the 10 ps data, as the model would have become unreliable due to an even lower photoactivation yield. We focus our discussion on monomer A and the 1 ps time point, although all conclusions are supported by monomer B and the features observed in the difference maps at 10 ps (*Table 2*, *Figure 1—figure supplement 5*).

First, we inspect the D-ring region at 1 ps (*Figure 3*). We observe strong negative difference density features on the atoms of the D-ring (marked I, II, III), correlating with density gains at both faces of the ring (IV, V, VI). These features strongly indicate that the D-ring twists. The positive feature IV homes the N-H and C = O groups, whereas V and VI indicate densities for the methyl and vinyl groups in the twisted ring (*Figure 3c*). Excellent agreement was obtained between the observed difference map and the difference map calculated from $DrBphP_{1ps}$ ($F_c^{1ps} - F_c^{dark}$), when the D-ring twists (C14-C15-C16-ND) from around 20° in the dark to 60° monomer A) and 90° monomer B) at 1 ps (*Figure 3c and e*). Although the twisting movement is clearly indicated by the difference map, we judge the precision of the angle to be low and approximately $\pm 25^\circ$.

Concomitant with the twist of the D-ring, the C-ring translates by approximately 0.69 Å as indicated by the correlated negative (VII) and positive (VIII) electron density (Figure 3a). Furthermore, the C-ring propionate chain detaches from its conserved anchoring residues Ser272 and Ser274 (IX and X, Figure 3a). The strictly conserved His260 retracts from its position (XI and XII) and Tyr263 moves upward at 1 ps (XIII and XIV, Figure 3b). The water network connecting the C-ring propionate, the D-ring C = O, and His290 rearranges accordingly (Figure 3a). The excellent agreement between calculated and observed difference maps confirms these observations (Figure 3d and e, Figure 3—figure supplement 2). We conclude that the twist of the D-ring causes detachment of the C-ring propionate from the protein scaffold by dislocation of the C-ring, facilitated by the associated hydrogen bonding network.

Turning our attention to the B-ring, we find that the B-ring propionate breaks its salt bridge to Arg254 (*Figure 3—figure supplement 3*). However, this is not caused by movements of the chromophore backbone, as we observe little change on the B-ring itself. Instead, we find that a water bridge between the B- and C-ring propionates is broken as indicated by negative difference electron densities on the waters (*Figure 3—figure supplement 3*). Additionally, the highly conserved helix from Ser257 to Val269, moves away from the chromophore by an average of 0.36 Å in monomer A and 0.62 Å in monomer B (distances relative to the pyrrole water, *Figure 3—figure supplement 4*). The



Table 1. Crystallographic table.

Table 1. Crystallographic tabl	e.		
	Dark	one ps	10 ps
PDB code	6T3L	6T3U	
Data collection			
Temperature (K)	293	293	293
Space Group	P212121	P212121	P212121
Cell dimensions (a, b, c)			
a, b, c (Å)	54.98 116.69 117.86	54.98 116.69 117.86	54.98 116.69 117.86
α, β, γ (°)	90.0 90.0 90.0	90.0 90.0 90.0	90.0 90.0 90.0
Data resolution overall (Å)‡	45.77–2.07	41.46–2.21	45.77–2.14
	(2.10–2.07)	(2.25–2.21)	(2.17–2.14)
R_{split} (%) $^{\dagger^{\dagger}}$	5.79 (120.05)	10.59 (114.64)	5.70 (121.86)
SNR $(I/\sigma(I))^{\ddagger}$	9.21 (0.83)	6.10 (0.88)	10.11 (0.99)
CC(1/2) [‡]	0.99 (0.33)	0.98 (0.38)	0.99 (0.344)
Completeness (%)‡	100 (100)	100 (100)	100 (100)
Multiplicity‡	461.35 (65.9)	106.11 (34.3)	347.36 (62.1)
Number of hits	149074	42853	159997
Number of indexed patterns	70726	21150	70335
Indexing rate(%)@sectionsign	47.44	49.35	43.96
Number of total reflections	24017763	5310179	17823530
Number of unique reflections	52060	39316	43279
Refinement			
Resolution (Å) [‡]	45.82–2.07	36.94–2.21	
	(2.12–2.07)	(2.27–2.21)	
R_{work} / R_{free}^{\ddagger}	0.162/0.191	0.230/0.256	
	(0.317/0.346)	(0.411/0.443)	
Number of atoms	5123	5135	
Average B factor (Å2)	76.44	78.63	
R.m.s deviations			
Bond lengths (Å)	0.007	0.006	
Bond angles (°)	1.251	1.152	

 $[\]uparrow \, \mathsf{R_{split}} = 1/\sqrt{2 \, \frac{\Sigma hkl|Ieven-Iodd|}{1/2\Sigma hkl|Ieven+Iodd|}}$.

changes of the D-ring are transduced to Ser257 via the side chains of His260 and Tyr263, and as a result, the hydrogen bond of Ser257 to the B-ring propionate group breaks. The amino acids in the stretch are over 50% conserved (*Figure 3—figure supplement 4*), suggesting that it has evolved to transfer an ultrafast signal. We conclude that relaxation of the protein is necessary for the detachment of the B-ring propionate from the protein scaffold.

Next to the changes around the D-ring, the maps reveal strong difference electron density on the A-ring (XVIII and XIX), Asp207 (XX to XXIII) (*Figure 4a*) and the pyrrole water (XV) (*Figure 4b*). When interpreted and modelled as downward movement of the A-ring and Asp207 and photodissociation of the pyrrole water from the chromophore, excellent agreement between calculated and observed difference electron density is obtained (*Figure 4—figure supplement 1*). The A-ring is covalently attached to the protein backbone in phytochromes (*Song et al., 2014*), which renders complete isomerization impossible, but is sufficiently flexible to accommodate the proposed changes. The

[‡] Highest resolution shell is shown in parentheses.

[§] Ratio of the number of indexed images to the total number of hits.



Table 2. Difference electron density features listed for certain atoms.

Pyrrole Water (+) Alt. 1 XVI 4.8σ 4.2σ 3.0σ 3.4σ Pyrrole Water (+) Alt. 2 XVII 4.4σ 5.8σ 3.0σ 3.3σ D-ring D-ring Wethyl (-) I -4.2σ -7.3σ -6.4σ -5.1σ D-ring Methyl (-) II -4.3σ -3.5σ -2.9σ -4.9σ D-ring Winyl (-) III -4.0σ -4.8σ -3.5σ -3.4σ D-ring Whyl (+) IV 4.6σ 6.4σ 4.6σ 4.1σ D-ring Methyl (+) V 3.5σ 3.4σ - - D-ring Winyl (+) VI 4.1σ 4.6σ 3.4σ 2.6σ C-ring C-ring Winyl (+) VI 4.1σ 4.6σ 3.4σ 2.6σ C-ring C-ring (-) IX -6.4σ -5.8σ -5.9σ -4.7σ C-propionate (-) IX -6.9σ 6.4σ 7.4σ 4.9σ C-ring (-) VIII 4.9σ 5.2σ 3.2σ 5.4σ C-ring (-) XXI	Object	Label	1ps	1ps	10ps	10ps
Pyrrole Water (·) XV -8.2σ -9.4σ -5.0σ -6.5σ Pyrrole Water (+) Alt. 1 XVI 4.8σ 4.2σ 3.0σ 3.4σ Pyrrole Water (+) Alt. 2 XVII 4.4σ 5.8σ 3.0σ 3.3σ D-ring D-ring N-H/C = O (·) I -4.2σ -7.3σ -6.4σ -5.1σ D-ring Wethyl (·) III -4.3σ -3.5σ -2.9σ -4.9σ D-ring Whyl (·) III -4.0σ -4.8σ -3.5σ -3.4σ D-ring Whyl (·) IV 4.6σ 6.4σ 4.6σ 4.1σ D-ring Whyl (·) V 3.5σ 3.4σ - - D-ring Whyl (·) VI 4.1σ 4.6σ 3.4σ 2.6σ D-ring Whyl (·) VI 4.1σ 4.6σ 3.4σ 2.6σ C-ring (whyl (·) VI 4.1σ 4.6σ 3.4σ 2.6σ C-ring (·) VII -5.5σ -4.4σ -5.1σ -3.2σ C-ring (·) VII			А	В	А	В
Pyrrole Water (+) Alt. 1 XVI 4.8σ 4.2σ 3.0σ 3.4σ Pyrrole Water (+) Alt. 2 XVII 4.4σ 5.8σ 3.0σ 3.3σ D-ring D-ring Methyl (-) II -4.2σ -7.3σ -6.4σ -5.1σ D-ring Methyl (-) III -4.3σ -3.5σ -2.9σ -4.9σ D-ring Winyl (-) III -4.0σ -4.8σ -3.5σ -3.4σ D-ring Winyl (-) IV 4.6σ 6.4σ 4.6σ 4.1σ D-ring Whyl (+) V 3.5σ 3.4σ - - D-ring Whyl (+) VI 4.1σ 4.6σ 3.4σ 2.6σ C-ring Methyl (-) V	Pyrrole Water					
Pyrrole Water (+) Alt. 2 XVII 4.4σ 5.8σ 3.0σ 3.3σ D-ring D-ring N-H/C = O (-) I -4.2σ -7.3σ -6.4σ -5.1σ D-ring Methyl (-) II -4.3σ -3.5σ -2.9σ -4.9σ D-ring Vinyl (-) III -4.0σ -4.8σ -3.5σ -3.4σ D-ring WhH/C = O (+) IV 4.6σ 6.4σ 4.6σ 4.1σ D-ring Methyl (+) V 3.5σ 3.4σ - - D-ring Methyl (+) VI 4.1σ 4.6σ 3.4σ - - D-ring Methyl (+) VI 4.1σ 4.6σ 3.4σ - - D-ring Methyl (+) VI 4.1σ 4.6σ 3.4σ - - D-ring Methyl (+) VI 4.1σ 4.6σ 3.4σ 2.6σ C-ring Winjl (+) VI 4.1σ -5.8σ -5.9σ -4.7σ C-ring (-) XX -6.9σ 6.4σ 7.4σ -5.1σ	Pyrrole Water (-)	XV	-8.2σ	-9.4σ	-5.0σ	-6.5σ
D-ring N-H/C = O (·)	Pyrrole Water (+) Alt. 1	XVI	4.8σ	4.2σ	3.0σ	3.4σ
D-ring N-H/C = O (·) I -4.2σ -7.3σ -6.4σ -5.1σ D-ring Methyl (·) III -4.3σ -3.5σ -2.9σ -4.9σ D-ring Methyl (·) IIII -4.0σ -4.8σ -3.5σ -3.4σ D-ring N-H/C = O (+) IV 4.6σ 6.4σ 4.6σ 4.1σ D-ring Methyl (+) V 3.5σ 3.4σ - - D-ring Methyl (+) VI 4.1σ 4.6σ 3.4σ - D-ring Methyl (+) VI 4.1σ 4.6σ 3.4σ - D-ring Methyl (+) VI 4.1σ 4.6σ 3.4σ - - D-ring Vinyl (+) VII -5.8σ -5.9σ -4.7σ -5.1σ -3.2σ C-propionate (·) IX -6.4σ -5.8σ -5.9σ -4.7σ -3.2σ C-propionate (+) X 6.9σ 6.4σ 7.4σ 4.9σ C-propionate (+) X 6.9σ 6.4σ 7.4σ 4.9σ C-ring (+) VIII 4.9σ 5.2σ 3.2σ 5.4σ A-ring A-ring C = O (·) XVIII -4.3σ -4.7σ -3.6σ -2.9σ A-ring C = O (+) XIX 5.2σ 5.0σ 5.7σ 4.7σ His260 His260 Sidechain(-) XII -6.7σ -5.2σ -6.3σ -4.1σ His260 Sidechain(-) XII -6.9σ -7.0σ -4.7σ -6.2σ Tyr263 Tyr263 Tyr263 Sidechain(-) XIII -6.9σ -7.0σ -7.0σ -4.7σ -6.2σ -6.2σ Asp207 Sidechain(-) XXI -6.2σ -5.4ν -5.1σ -3.4σ Asp207 Sidechain(-) XXI -6.2σ -5.4ν -5.1σ -3.8σ -3.8σ Phe203	Pyrrole Water (+) Alt. 2	XVII	4.4σ	5.8σ	3.0σ	3.3σ
D-ring Methyl (·) II -4.3σ -3.5σ -2.9σ -4.9σ D-ring Vinyl (·) III -4.0σ -4.8σ -3.5σ -3.4σ D-ring N-H/C = O (+) IV 4.6σ 6.4σ 4.6σ 4.6σ 4.1σ D-ring Methyl (+) V 3.5σ 3.4σ - - D-ring Methyl (+) VI 4.1σ 4.6σ 3.4σ 2.6σ C-ring C-propionate (·) IX -6.4σ -5.8σ -5.9σ -4.7σ -3.2σ C-propionate (+) X 6.9σ 6.4σ 7.4σ 4.9σ C-ring (+) VIII 4.9σ 5.2σ 3.2σ 5.4σ A-ring C-propionate (+) XIX 5.2σ 5.0σ 5.7σ 4.7σ 4.7σ 4.7σ 4.7σ 4.7σ 7.7σ 7.7	D-ring					
D-ring Vinyl (·) III	D-ring N-H/C = O (-)	I	-4.2σ	-7.3σ	-6.4σ	-5.1σ
D-ring N-H/C = O (+) IV 4.6σ 6.4σ 4.6σ 4.1σ D-ring Methyl (+) V 3.5σ 3.4σ - - D-ring Vinyl (+) VI 4.1σ 4.6σ 3.4σ 2.6σ C-ring C-ring C-ring -5.8σ -5.9σ -4.7σ C-ring (-) VII -5.5σ -4.4σ -5.1σ -3.2σ C-ring (-) VIII -5.5σ -4.4σ -5.1σ -3.2σ C-propionate (+) X 6.9σ 6.4σ 7.4σ 4.9σ C-ring (+) VIII 4.9σ 5.2σ 3.2σ 5.4σ A-ring A-ring -4.7σ -3.6σ -2.9σ A-ring C = O (-) XVIII -4.3σ -4.7σ -3.6σ -2.9σ A-ring C = O (+) XIX 5.2σ 5.0σ 5.7σ 4.7σ His260 Sidechain(-) XI -6.7σ -5.2σ -6.3σ -4.1σ His260 Sidechain(-) XII 4.3σ 4.5σ 3.5σ <td>D-ring Methyl (-)</td> <td>II</td> <td>-4.3σ</td> <td>-3.5σ</td> <td>-2.9σ</td> <td>-4.9σ</td>	D-ring Methyl (-)	II	-4.3σ	-3.5σ	-2.9σ	-4.9σ
D-ring Methyl (+) V 3.5σ 3.4σ - - D-ring Vinyl (+) VI 4.1σ 4.6σ 3.4σ 2.6σ C-ring C-propionate (-) IX -6.4σ -5.8σ -5.9σ -4.7σ C-ring (-) VII -5.5σ -4.4σ -5.1σ -3.2σ C-propionate (+) X 6.9σ 6.4σ 7.4σ 4.9σ C-ring (+) VIII 4.9σ 5.2σ 3.2σ 5.4σ A-ring A-ring -4.7σ -3.6σ -2.9σ A-ring C = O (-) XVIII -4.3σ -4.7σ -3.6σ -2.9σ A-ring C = O (+) XIX 5.2σ 5.0σ 5.7σ 4.7σ His260 His260 Sidechain(-) XI -6.7σ -5.2σ -6.3σ -4.1σ His260 Sidechain(-) XII 4.3σ 4.5σ 3.5σ 3.2σ Tyr263 Sidechain(-) XIII -6.9σ -7.0σ -4.7σ -6.2σ Tyr263 Sidechain(-) XX	D-ring Vinyl (-)	III	-4.0σ	-4.8σ	-3.5σ	-3.4σ
D-ring Vinyl (+)	D-ring N-H/C = O (+)	IV	4.6σ	6.4σ	4.6σ	4.1σ
C-ring (-) IX	D-ring Methyl (+)	V	3.5σ	3.4σ	-	-
C-propionate (-) IX	D-ring Vinyl (+)	VI	4.1σ	4.6σ	3.4σ	2.6σ
C-ring (·) VII	C-ring					
C-propionate (+) X 6.9σ 6.4σ 7.4σ 4.9σ C-ring (+) VIII 4.9σ 5.2σ 3.2σ 5.4σ A-ring A-ring C = O (-) XVIII -4.3σ -4.7σ -3.6σ -2.9σ A-ring C = O (+) XIX 5.2σ 5.0σ 5.7σ 4.7σ His260 His260 Sidechain(-) XI -6.7σ -5.2σ -6.3σ -4.1σ His260 Sidechain(+) XII 4.3σ 4.5σ 3.5σ 3.2σ Tyr263 Sidechain(-) XII -6.9σ -7.0σ -4.7σ -6.2σ Tyr263 Sidechain(+) XIV 4.8σ 4.9σ 3.0σ 4.3σ Asp207 Asp207 Sidechain (-) XX -6.2σ -6.7σ -5.6σ -3.4σ Asp207 Sidechain(+) XXI 5.7σ 5.0σ 4.2σ - Asp207 Backbone (-) XXII -6.2σ -5.4ν -5.1σ -4.5σ Tyr176 Sidechain(-) -4.9σ -3.9σ -5.1σ -3.8σ Phe203	C-propionate (-)	IX	-6.4σ	-5.8σ	-5.9σ	-4.7σ
C-ring (+) VIII 4.9σ 5.2σ 3.2σ 5.4σ A-ring A-ring C = O (-) XVIII -4.3σ -4.7σ -3.6σ -2.9σ A-ring C = O (+) XIX 5.2σ 5.0σ 5.7σ 4.7σ His260 His260 Sidechain(-) XI -6.7σ -5.2σ -6.3σ -4.1σ His260 Sidechain(+) XII 4.3σ 4.5σ 3.5σ 3.2σ Tyr263 Tyr263 Sidechain(-) XIII -6.9σ -7.0σ -4.7σ -6.2σ Tyr263 Sidechain(+) XIV 4.8σ 4.9σ 3.0σ 4.3σ Asp207 Asp207 Sidechain (-) XX -6.2σ -6.7σ -5.6σ -3.4σ Asp207 Backbone (-) XXII 5.7σ 5.0σ 4.2σ - Asp207 Backbone (-) XXII -6.2σ -5.4v -5.1σ -4.5σ Asp207 Backbone (-) XIII 4.6σ 4.4σ 4.5σ 3.5σ Tyr176 Tyr176 Sidechain(-) -4.9σ -3.9σ -5.1σ -3.8σ Phe203 -5.4σ -5.1σ -5.1σ	C-ring (-)	VII	-5.5σ	-4.4σ	-5.1σ	-3.2σ
A-ring C = O (-) XVIII	C-propionate (+)	Х	6.9σ	6.4σ	7.4σ	4.9σ
A-ring C = O (-) XVIII	C-ring (+)	VIII	4.9σ	5.2σ	3.2σ	5.4σ
A-ring C = O (+) XIX 5.2σ 5.0σ 5.7σ 4.7σ His260 His260 Sidechain(-) XI -6.7σ -5.2σ -6.3σ -4.1σ His260 Sidechain(+) XII 4.3σ 4.5σ 3.5σ 3.2σ Tyr263 Tyr263 Sidechain(-) XII -6.9σ -7.0σ -4.7σ -6.2σ Tyr263 Sidechain(+) XIV 4.8σ 4.9σ 3.0σ 4.3σ Asp207 Asp207 Sidechain (-) XX -6.2σ -6.7σ -5.6σ -3.4σ Asp207 Sidechain(+) XXI 5.7σ 5.0σ 4.2σ - Asp207 Backbone (-) XXII -6.2σ -5.4ν -5.1σ -4.5σ Asp207 Backbone (+) XIII 4.6σ 4.4σ 4.5σ 3.5σ Tyr176 Tyr176 Sidechain(-) -4.9σ -3.9σ -5.1σ -3.8σ Phe203	A-ring					
His260 Sidechain(-) XI	A-ring $C = O(-)$	XVIII	-4.3σ	-4.7σ	-3.6σ	-2.9σ
His260 Sidechain(-) XI	A-ring $C = O(+)$	XIX	5.2σ	5.0σ	5.7σ	4.7σ
His260 Sidechain(+) XII 4.3σ 4.5σ 3.5σ 3.2σ Tyr263 Tyr263 Sidechain(-) XIII -6.9σ -7.0σ -4.7σ -6.2σ Tyr263 Sidechain(+) XIV 4.8σ 4.9σ 3.0σ 4.3σ Asp207 Asp207 Sidechain (-) XX -6.2σ -6.7σ -5.6σ -3.4σ Asp207 Sidechain(+) XXI 5.7σ 5.0σ 4.2σ - Asp207 Backbone (-) XXII -6.2σ -5.4v -5.1σ -4.5σ Asp207 Backbone (+) XIII 4.6σ 4.4σ 4.5σ 3.5σ Tyr176 -4.9σ -3.9σ -5.1σ -3.8σ Phe203	His260					
Tyr263 Sidechain(-) XIII	His260 Sidechain(-)	XI	-6.7σ	-5.2σ	-6.3σ	-4.1σ
Tyr263 Sidechain(-) XIII	His260 Sidechain(+)	XII	4.3σ	4.5σ	3.5σ	3.2σ
Tyr263 Sidechain(+) XIV 4.8σ 4.9σ 3.0σ 4.3σ Asp207 Asp207 Sidechain (-) XX -6.2σ -6.7σ -5.6σ -3.4σ Asp207 Sidechain(+) XXI 5.7σ 5.0σ 4.2σ - Asp207 Backbone (-) XXII -6.2σ -5.4ν -5.1σ -4.5σ Asp207 Backbone (+) XIII 4.6σ 4.4σ 4.5σ 3.5σ Tyr176 Tyr176 Sidechain(-) -4.9σ -3.9σ -5.1σ -3.8σ Phe203	Tyr263					
Asp207 Asp207 Sidechain (-) XX -6.2σ -6.7σ -5.6σ -3.4σ Asp207 Sidechain(+) XXI 5.7σ 5.0σ 4.2σ - Asp207 Backbone (-) XXII -6.2σ -5.4v -5.1σ -4.5σ Asp207 Backbone (+) XIII 4.6σ 4.4σ 4.5σ 3.5σ Tyr176 Tyr176 Sidechain(-) -4.9σ -3.9σ -5.1σ -3.8σ Phe203	Tyr263 Sidechain(-)	XIII	-6.9σ	-7.0σ	-4.7σ	-6.2σ
Asp207 Sidechain (-) XX -6.2σ -6.7σ -5.6σ -3.4σ Asp207 Sidechain(+) XXI 5.7σ 5.0σ 4.2σ - Asp207 Backbone (-) XXII -6.2σ -5.4v -5.1σ -4.5σ Asp207 Backbone (+) XIII 4.6σ 4.4σ 4.5σ 3.5σ Tyr176 -4.9σ -3.9σ -5.1σ -3.8σ Phe203	Tyr263 Sidechain(+)	XIV	4.8σ	4.9σ	3.0σ	4.3σ
Asp207 Sidechain(+) XXI 5.7σ 5.0σ 4.2σ - Asp207 Backbone (-) XXII -6.2σ -5.4v -5.1σ -4.5σ Asp207 Backbone (+) XIII 4.6σ 4.4σ 4.5σ 3.5σ Tyr176 Tyr176 Sidechain(-) -4.9σ -3.9σ -5.1σ -3.8σ Phe203	Asp207					
Asp207 Backbone (-) XXII -6.2σ -5.4v -5.1σ -4.5σ Asp207 Backbone (+) XIII 4.6σ 4.4σ 4.5σ 3.5σ Tyr176 -4.9σ -3.9σ -5.1σ -3.8σ Phe203	Asp207 Sidechain (-)	XX	-6.2σ	-6.7σ	-5.6σ	-3.4σ
Asp207 Backbone (+) XIII 4.6σ 4.4σ 4.5σ 3.5σ Tyr176 Tyr176 Sidechain(-) -4.9σ -3.9σ -5.1σ -3.8σ Phe203 Phe203 -4.9σ -3.9σ -5.1σ -3.8σ	Asp207 Sidechain(+)	XXI	5.7σ	5.0σ	4.2σ	-
Tyr176 Tyr176 Sidechain(-)	Asp207 Backbone (-)	XXII	-6.2σ	-5.4v	-5.1σ	-4.5σ
Tyr176 Sidechain(-) -4.9σ -3.9σ -5.1σ -3.8σ Phe203	Asp207 Backbone (+)	XIII	4.6σ	4.4σ	4.5σ	3.5σ
Phe203	Tyr176					
	Tyr176 Sidechain(-)		-4.9σ	-3.9σ	-5.1σ	-3.8σ
Phe203 Sidechain(-) -4.1σ -4.6σ -4.6σ -	Phe203					
	Phe203 Sidechain(-)		-4.1σ	-4.6σ	-4.6σ	-

pyrrole water may either move to feature (XVI), or occupy an anisotropic, worm-shaped feature which extends from the A-ring to the D-ring (XVII) (*Figure 4b*).

Furthermore, correlated negative and positive electron density features are observed on backbone atoms of the highly conserved stretch from Pro201 to His209. These difference electron density features indicate that the residues move away from the centre of the chromophore by an average of 0.54 Å and 0.57 Å in monomers A and B, respectively (*Figure 3—figure supplement 4b*). The stretch includes Asp207 and it is located between the A-ring and the PHY domain, which makes it plausible that the changes in the chromophore cause this protein rearrangement. The



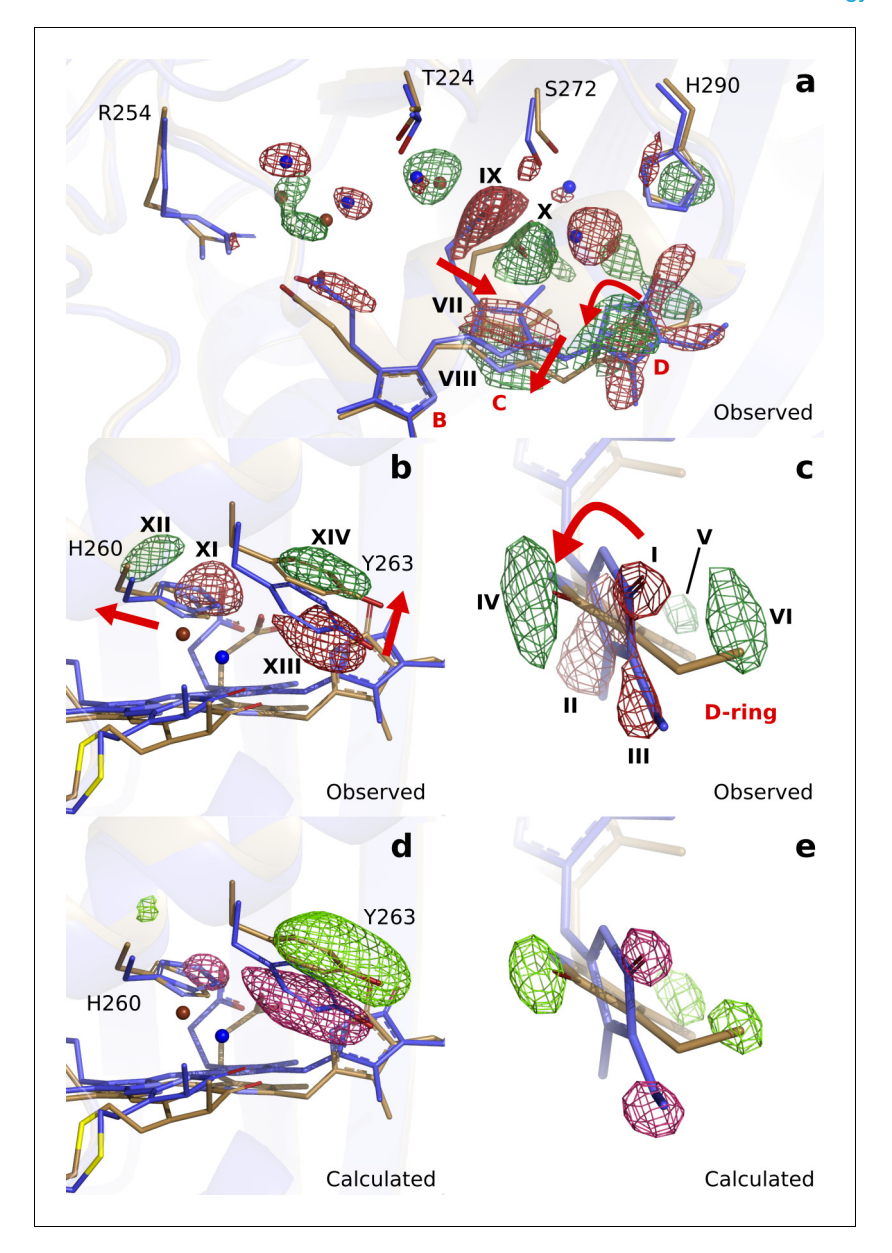


Figure 3. Observed and calculated difference electron densities reveal a twist of the D-ring and significant protein rearrangements. The observed difference electron density with the refined $DrBphP_{dark}(blue)$ and $DrBphP_{1ps}(beige)$ structures, shown for (a) the B-, C-, and D-ring surroundings, (b) the strictly conserved His260 and Tyr263, and (c) the D-ring. The calculated difference electron density shown for (d) His260 and Tyr263 and (e) the D-ring. The D-ring twists counter-clockwise when viewed along C15-C16 bond toward the C-ring. The observed difference electron density is contoured at 3.3 σ. And the calculated difference electron density is contoured at 3.5 and 5.0 σ for panel d and e, respectively. Monomer A is shown in this figure.

The online version of this article includes the following figure supplement(s) for figure 3:

Figure supplement 1. Extrapolated maps at $\alpha=25$ demonstrate that the D-ring twists in the photoactivated state.

Figure supplement 2. Comparison of observed (upper panel) and calculated (lower panel) difference electron densities indicate good agreement around the B-D rings.

Figure supplement 3. Hydrogen bonding network between the chromophore propionate groups is disrupted at 1 ps delay time.

Figure supplement 4. Backbone movements at 1 ps.



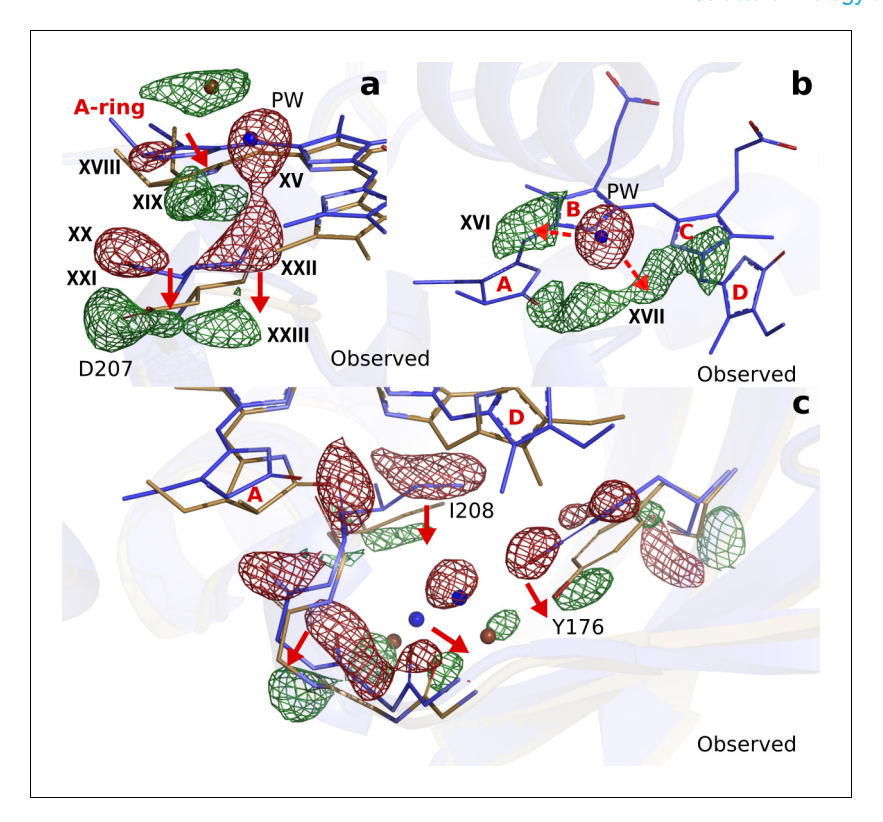


Figure 4. Photodissociation of the pyrrole water, displacement of the A-ring and its effect on the proteins scaffold. (a). The observed difference electron density displayed with the $DrBphP_{dark}$ (blue) and $DrBphP_{1ps}$ (beige) structures around the A-ring, Asp207 and pyrrole water (PW). The structural model was inconclusive as to whether the A-ring twists around the double bond between the B- and A-ring, or whether it tilts downward hinged on the connection between C- and B-ring. (b). The regions of the pyrrole water (PW) and the area between the pyrrole rings show negative and positive densities, respectively. The observed difference electron density is contoured at 3.3σ . (c). Density displayed for the backbone below the A-ring, including side chains of the strictly conserved Ile208 and Tyr176 as well as the surrounding water network. Monomer A is shown in this figure.

Figure supplement 1. Comparison of observed and calculated difference electron densities in the A-ring region.

changes are complemented by significant rearrangements of a stretch of waters and a conserved Tyr176 (*Figure 4c*).

Discussion

The structure of DrBphP_{CBD} 1 ps after photoexcition reveals changes of the biliverdin chromophore and the surrounding residues. We find a twist of the D-ring, displacement of the C-ring, and associated changes of the water network which connects the D-ring, the C-ring propionate, and His290. Further, we identify a disruption of the salt bridge between the B-ring propionate and the Arg254, and significant changes around the A-ring, Asp207 and the pyrrole water. The changes are retained at 10 ps, even though at a lower population (Figure 1—figure supplement 5). The extensive and coordinated structural changes in the binding pocket (Figure 3) manifest a liberation of the chromophore from the protein scaffold, which we propose to be necessary for the conformational rearrangements to occur in the downstream photoconversion to Pfr.

Infrared spectral data indicate significant reorganization of the chromophore and several amino acids including the PHY-tongue region as early as in Lumi-R state, which is the first known ground state intermediate in the photoconversion from Pr to Pfr (*Ihalainen et al., 2018*; *van Thor et al., 2007*). However, the structure of the bilin and the binding pocket in Lumi-R is not known, because structural information is missing. Since the quantum yield of reaching the Lumi-R state is low (on the



order of 10%), spectroscopic investigation of the mechanism is difficult, and it is currently not fully established how the Lumi-R state is reached. Crystallographic data does not report on whether the chromophore is electronically excited or not, hence we cannot determine whether the structure that we observe is in a relaxed excited state or in a ground state. The time delay (1 ps) supports that our structure presents an intermediate enroute to the Lumi-R state.

The D-ring of the bilin chromophore isomerizes around the C15-C16 bond from (Z) in Pr to (E) in Pfr (*Rüdiger et al., 1983*; *Burgie et al., 2016*; *Takala et al., 2014*; *Yang et al., 2008*; *Essen et al., 2008*). Circular dichroism spectroscopy and solid-state NMR spectroscopy have indicated that the position of the D-ring inverts from an ' α '-facial (Pr) to a ' β '-facial (Pfr) position in cyanobacterial and plant phytochromes, whereas it stays ' α '-facial in bacterial phytochromes (*Rockwell et al., 2009*; *Song et al., 2011*; *Song et al., 2018*). Based on anticipated steric clashes with the C-ring methyl group, it has been proposed that the D-ring rotates counter-clockwise in plant and cyanobacterial phytochromes, but clockwise in bacterial phytochromes (*Rockwell et al., 2009*). Moreover, spectroscopy has shown that the D-ring of the bilin chromophore is already isomerized in the Lumi-R state (*van Thor et al., 2007*; *Heyne et al., 2002*; *Yang et al., 2012*).

Seemingly contradictory, we now observe that the D-ring is rotated counter-clockwise by tens of degrees for the bacterial DrBphP at 1 ps time delay (Figure 3c and e). The conformation is strongly supported by the difference map. It contains two positive peaks (V and VI in Figure 3c), which indicate the new position of the vinyl and methyl group of the D-ring. We tested models in which the D-ring was rotated in a clockwise direction, but the agreement with the experimental difference map decreased. Thus, it may be that the D-ring indeed rotates counter-clockwise in bacterial phytochromes, similar to plant and cyanobacterial phytochromes. For complete isomerization, this would mean that the C-ring moves out of the way during the rotation. We observe significant movements of the C-ring, which may be an indication for that such a mechanism is possible. Raising a note of caution, we cannot fully exclude that the truncation of our phytochrome construct or the crystal packing influences the direction of rotation. NMR studies have reported conformational heterogeneity in the chromophore binding pocket of phytochromes in solution (Song et al., 2011; Lim et al., 2018; Song et al., 2018; Gustavsson et al., 2020). Crystallization could select one of the conformations, which may have a preferred rotation in the counter-clockwise direction. More experiments are needed to clarify this question.

It is interesting to compare the structural changes at 1 ps time delay to the changes observed in the conversion between Pr and Pfr (Burgie et al., 2016; Takala et al., 2014; Stojković et al., 2014). Major changes include a flipped D-ring, changes in conserved residues of the chromophore-binding pocket, for example Tyr176, His201 and Phe203, and refolding of the PHY tongue. The PHY tongue is not included in our construct, but Tyr176 and Phe203 are associated with difference electron density features in our maps (Table 2). However, the movements are much smaller at 1 ps compared to the Pr-to-Pfr transition. This is not unexpected, given the short time delays, but it shows that the residues are tightly coupled to the chromophore. Interestingly, the Pr and Pfr structures also reveal a sliding movement of the entire chromophore (Yang et al., 2011; Burgie et al., 2016; Takala et al., 2014). This requires that the propionic groups have to break their bonds to the protein scaffold. Our data indicate that this is part of the primary photoresponse.

The photodissociation of the pyrrole water from the chromophore is a surprising finding. The pyrrole water is ubiquitously found in phytochrome structures (Essen et al., 2008; Yang et al., 2008; Otero et al., 2016; Burgie et al., 2016; Wagner et al., 2005; Burgie et al., 2014; Schmidt et al., 2018; Yang et al., 2011). Our fluence dependent SFX data show that the negative density on the pyrrole water is the last signal to disappear when lowering the photon excitation densities 10-fold (Figure 2). This makes us confident that the photodissociation reaction is not caused by multi-photon effects. The removal of the water requires significant energy, because the hydrogen bonds to the A-, B-, and C-rings of the chromophore and the backbone C = O group of Asp207 have to be broken. We do not think that the twist of the D-ring causes this through direct steric interactions, because there is no contact between the pyrrole water and the D-ring. Rather, it may be triggered by an excited state charge redistribution between the pyrrole water and the chromophore, for example by ultrafast proton or electron transfer (Toh et al., 2010). Such charge re-distributions are typically facilitated by changes in geometry (Nosenko et al., 2008) and may therefore be caused indirectly by structural changes of the A-, C-, or D-rings, but this requires further investigation.



Conformational changes of the A-ring, Asp207 and the pyrrole water have not been considered to occur on picosecond time scales. The strictly conserved Asp207 is a key residue for signal transduction because it connects the chromophore to the PHY-tongue in Pr and Pfr (*Essen et al., 2008*; *Yang et al., 2008*; *Takala et al., 2014*). Its displacement suggests, together with the relocation of the residue stretch surrounding it, that disruption of the GAF-PHY interface may occur as early as 1 ps after photoexcitation (*Figure 3—figure supplement 4b*). With a hydrogen bond to the pyrrole water and in tight steric contact with the A-ring, Asp207 thereby acts as an extended arm of the chromophore. We propose that the photodissociation of the pyrrole water from the bilin and the change of the A-ring are integral parts of ultrafast phytochrome signaling toward the PHY domain.

We demonstrate that within 1 ps, the D-ring twists, that the chromophore is liberated from the protein (*Figure 5a*) and that movements of the pyrrole water, the A-ring and Asp207 lead to signaling directed toward the PHY-tongue (*Figure 5b*). When mapped on the structure of the complete photosensory core module (*Takala et al., 2014*), both changes work together to destabilize the Arg466:Asp207 salt bridge. Tyr263 moves up, caused by the twist of the D-ring, and Asp207 moves down, caused by changes of the A-ring, retracting both residues from the salt bridge.

Our data reveal a highly collective primary photoresponse for phytochromes. This is consistent with the fact that most point mutations of conserved residues alter, but do not inhibit, photoconversion (*Wagner et al., 2008*). The ultrafast structural changes are more extensive than in bacteriorhodopsin, photoactive yellow proteins, and in a fluorescent protein (*Pande et al., 2016*; *Nogly et al., 2018*). While previously observed ultrafast backbone movements have been interpreted as 'protein quakes' for myoglobin and bacteriorhodopsin (*Barends et al., 2015*; *Nogly et al., 2018*; *Toh et al., 2010*), the present backbone motion in the phytochrome binding pocket are much more directed (*Figure 3—figure supplement 4*). The changes occur in highly conserved regions of the protein and are part of the collective signaling response of the entire binding pocket.

Phytochromes have to be able to stabilize the bilin and to direct its photoisomerization from two photochemical ground states, Pr and Pfr. These differ both structurally and electronically, which precludes a single reaction trajectory for isomerization in the two directions. With this in mind, the observed primary photoresponse is reasonable. The structural signal is highly delocalized already at 1 ps, causing near-simultaneous liberation of the chromophore and initial signal transduction. We propose that these reaction trajectories stabilize each other, navigating the protein into a productive

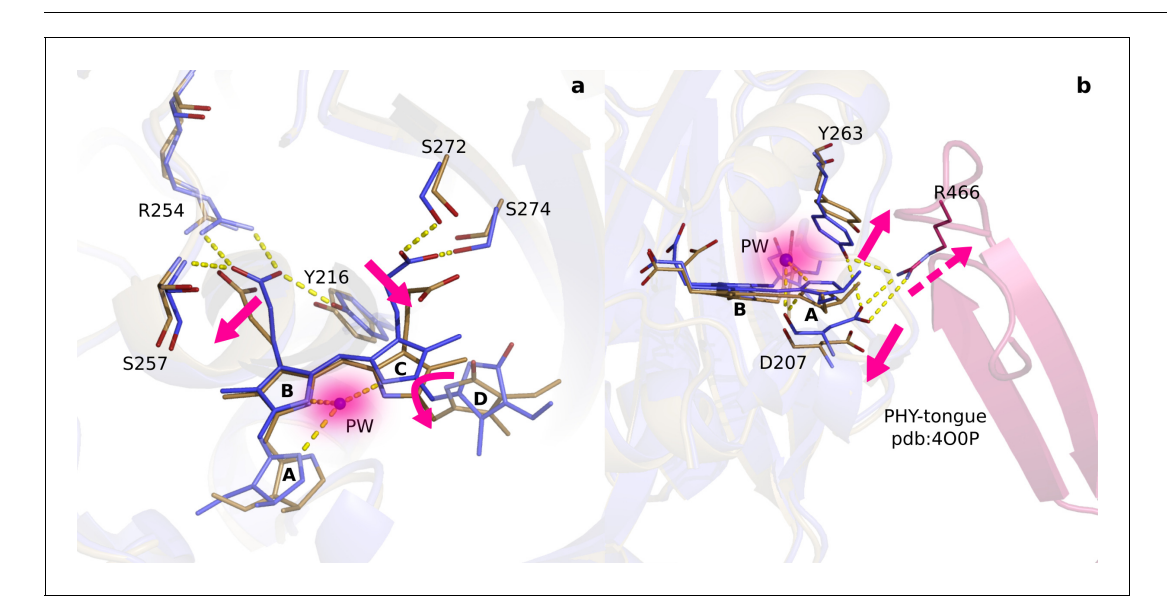


Figure 5. Two correlated photochemical events guide the primary photorespone of phytochrome proteins. (a). The structures (*Dr*BphP_{dark}, blue and *Dr*BphP_{1ps}, beige) indicate that rotation of the D-ring initiates breakage of non-covalent bonds of the propionates to the protein scaffold. Even the C-and A-rings are displaced significantly and the pyrrole water is dislocated from its original location at 1 ps (shade). (b). The same structures are overlayed with the complete photosensory core in Pr state (PDB ID 400P, pink) (*Takala et al., 2014*). The scissor-like separation of Asp207 and Tyr263 could result in breakage of the hydrogen bonds to Arg466 of the conserved PRXSF motif located in the PHY-tongue region.



reaction path. The multidimensional reaction trajectory is consistent with the low quantum yields for photoconversion (*Lamparter et al.*, 1997), which are characteristic for the phytochrome superfamily. Whereas the twisting motion of the D-ring has been the working model for phytochrome activation and is now confirmed, the photodissociation of the pyrrole water is highly surprising. We propose that both chemical events work together and enable phytochrome proteins to translate light information into structural signals, guiding the growth and development of plants, fungi, and bacteria on Earth.

Materials and methods

Protein purification and crystallization

The *His*₆-tagged PAS-GAF domain from *D. radiodurans* (aa 1–321) in vector pET21b(+) (*Wagner et al., 2005*) was expressed and purified as previously described (*Lehtivuori et al., 2013*; *Takala et al., 2014*). The recombinant protein was expressed in *Escherichia coli* strain BL21(DE3), either with or without *Ho*1 to yield holo- or apoprotein, respectively. Cells were lysed with Emulsiflex and cleared by centrifugation (20,000 rpm, 30 min, +4°C). Full biliverdin incorporation was ensured by adding 8 mg of biliverdin hydrochloride (Frontier Scientific) per litre of cell culture to the cell lysate, followed by overnight incubation on ice. The protein was then purified at room temperature with HisTrap HP column (GE Healtcare) in 30 mM Tris, 50 mM NaCl and 5 mM imidazole (pH 8) and eluted with increasing imidazole concentration (gradient elution over 5–500 mM). Size-exclusion chromatography was then conducted with a HiLoad 26/600 Superdex 200 pg column (GE Healthcare) in buffer (30 mM Tris pH 8.0). Finally, the protein was concentrated to 30–50 mg/mL and flashfrozen in liquid nitrogen.

Crystals were set up under green safe light and grown in dark. Batch crystallization was performed as described (*Edlund et al., 2016*). 50 μ L of purified protein (25–30 mg/mL) was added to 450 μ L of reservoir solution (60 mM Sodium acetate pH 4.95, 3.3% PEG 400, 1 mM DTT and 30% 2-methyl-2,4-pentanediol) and immediately mixed. Initial microcrystals were grown on a tipping table at 4 °C for 48 hr. Once the microcrystals were formed, additional protein was added to increase crystal size. The microcrystals were first pelleted by brief centrifugation and 400 μ L of supernatant was removed. 200 μ L of diluted protein (14 mg/mL in 30 mM Tris pH 8.0) was then added to the microcrystals along with 200 μ L of fresh reservoir solution. After 48 hr incubation on a tipping table at room temperature, crystals of diffraction quality (20–70 μ m long needles) were formed (*Figure 1*—*figure supplement 2* and *Table 1*).

Transient absorption experiment of microcrystals

Transient absorption experiments were performed on a home build setup based on a Ti:sapphire femtosecond laser system (1 kHz, 800 nm). The main beam was split into pump and probe beams. The pump beam was sent through the home build noncollinear optical parametric amplifier to produce excitation pulses at 640 nm central wavelength. The probe beam was focused on a 2 mm sapphire plate to generate broadband (400–760 nm) white light which was split by 50/50 beamsplitter to reference and probe beams. The mutual polarization of the pump and probe beams was set to the magic angle (54.7°) by Berek compensator. The probe beam was focused on a sample cuvette that was continuously translated in vertical axis to prevent sample degradation. The microcrystals were washed with crystallization buffer five time in order to remove the solubilized proteins. 2.5 μ L of microcrystals including a small amount of crystallization buffer were placed between two CaF₂ windows without a spacer. The OD of the sample was about 0.6. Time-resolved absorption changes were measured by detecting probe and reference beams dispersed on the double-diode array; the time delay between pump and probe pulses was set by a computer controlled delay line placed in the probe beam path. All measurements were carried out in room temperature.

Light scattering of the grease jet

In order to estimate the light intensity of the optical laser in the grease jet, the optical transmission of the grease, grease mixed with crystallization buffer, microcrystals in the grease matrix and pure microcrystals were measured with a transmittance diode-array UV-Vis spectrometer (Cary 8454, Agilent Technologies) (*Figure 1—figure supplement 1c*). 2.5 µl each of sample was placed between



two CaF_2 windows with a 50 μ m Teflon spacer and squeezed together, resembling the characteristics of the jet during the XFEL experiments. The raw spectra of microcrystals (*Figure 1—figure supplement 1c*) in the buffer has been measured between two CaF_2 windows without spacer to minimize the absorption loss, the pathlength was estimated to be $\leq 50\mu$ m.

Fluence calculations

The optical laser parameters used for the experiment were as follows: wavelength was 640 nm, the laser-spot dimensions at the focus was 100 \times 80 μm^2 FWHM (170 \times 136 μm^2 at $1/e^2$ intensity), the pulse energy was 40 µJ, the nominal pulse duration was 70 fs (not confirmed at the sample position), and the repetition rate was 30 Hz. The energy of a photon at 640 nm is 3.1×10^{-19} J. Using the photon density of the laser at $1/e^2$ convention of 1.7 mJ/mm², we obtain a photon fluence of $5.48 \times 10^{15} \mathrm{photons \cdot mm^{-2}}$. The extinction coefficient of biliverdin in the phytochrome at 640 nm (ϵ_{640}) $27.7 \times 10^3 \sim M^{-1} cm^{-1}$ and the cross section $\sigma_{640} = ln(10) \cdot \epsilon_{640} \cdot 1000/N_A = 1.06 \times 10^{-14} \sim \text{mm}^2 \cdot \text{molecule}^{-1}$, where N_A is Avogadro's number. Multiplying the photon fluence with the cross section yields 58 photons per molecule. Light scattering in the carrier matrix decreases the effective fluence of photons that interact with the crystals. Our absorption spectra of the grease (Figure 1-figure supplement 1) indicate that the grease is transparent when untreated, but attenuates the light intensity by 2 orders of magnitude in the visible region when mixed with crystallization buffer or crystals (pathlength 50 μm). This indicates that almost every photon is scattered. Therefore, even when neglecting the scattering of the jet surface, crystals will be exposed to a photon fluence that is significantly reduced. A reduction of the photon fluence by 2 orders of magnitude is a realistic assumption as we used grease jets with a diameter of $75 \mu m$ or $100 \mu m$. Another factor that contributes to the reduction of the number of photons per chromophore and non-homogeneous illumination of the microcrystals is the orientation of the crystals and the high chromophore density in them. The first few chromophores in the light path will shade the remaining chromophores in the needle-shaped crystals. Since the X-rays probe every molecule in their path with approximately same likelihood, the average photon fluence per probed chromophore is reduced. Assuming that the effective fluence inside the grease jet is reduced by a factor of 100, we estimate an average number of 0.5-1 photons per chromophore. This is consistent with the photoexcitation yield of 8% and with our experimental finding that the difference signal vanishes under the noise signal when reducing the photon fluence by a factor of 10 (Figure 2).

SFX data acquisition

Serial femtosecond crystallographic data were collected at SPring-8 Angstrom Compact Free Electron Laser (SACLA) in two beamtimes in October 2018 and May 2019. The microcrystals were pelleted by brief centrifugation and the crystal pellet was mixed with 180 μ L of grease. The grease/crystal mixture was loaded into a 4 mm sample reservoir for data acquisition. The sample was delivered to the X-ray beam at a flow rate of 2.5 μ L/min or 4.2 μ L/min for 75 μ m and 100 μ m diameter nozzles, respectively. The time resolution of the experiment was limited by the jitter of the XFEL of 100 fs *r.m.s.* The experimental settings were nominally the same for the 1 ps and 10 ps delay times and all data were recorded during 7 hr of beamtime. We also recorded data at 3 ps delay time, but these generated electron density maps of poor quality due to an unknown reason and were therefore not analyzed further.

Data processing

The background of the detector was estimated by averaging the first 150 dark images in each run and then subtracted from each diffraction pattern. Diffraction images with Bragg spots (the 'hits') were found by a version of Cheetah adapted for SACLA (*Nakane et al., 2016*; *Barty et al., 2014*). These hits were indexed by the program CrystFEL (version 0.6.3) (*White et al., 2012*). Indexing was performed using Dirax and Mosflm (*Duisenberg, 1992*; *Battye et al., 2011*). Spot finding in each diffraction image was done with the peakfinder8 algorithm using the parameters (min SNR = 4.5, threshold = 100, minimum pixel counts = 3). The indexed patterns were merged and scaled using partialator in CrystFEL and hkl files were produced. The figure of merits (*Table 1*) were calculated by using compare_hkl and check_hkl in CrystFEL. The histograms of the unit cell parameters are presented in *Figure 3*. All diffraction images have been deposited to CXIDB under ID 121.



Refinement of dark structure

The initial phases were solved by molecular replacement with Phaser (*McCoy* et al., 2007) and the PAS-GAF crystal structure (PDB ID 5K5B) (*Edlund* et al., 2016) as a search model. The structure was refined with REFMAC version 5.8.0135 (*Murshudov* et al., 2011) with a weight factor for the geometry restraints of 0.05, accompanied by model building steps with Coot 0.8.2 (*Emsley* et al., 2010). The final structure (*Dr*BphP_{dark}) had Rwork/Rfree of 0.161/0.192 and no Ramachandran outliers (*Table* 1). The coordinates and structure factors have been deposited in the Protein Data Bank under the accession code 6T3L.

Computation of difference electron density maps

The difference structure factors (ΔF) are computed from the measured structure factor amplitudes in dark and for preset delay times between laser and X-ray pulses as $|\Delta F_o| = w(|F_o^{light}| - |F_o^{dark}|)$ and with phases taken from the dark structural model ($DrBphP_{dark}$). $|F_o^{dark}|$ and $|F_o^{light}|$ were brought to the absolute scale by first scaling $|F_o^{dark}|$ to $|F_c^{dark}|$ and then scaling $|F_o^{light}|$ to $|F_o^{dark}|$ using the CCP4 program Scaleit (Winn et al., 2011). Difference Fourier density maps were calculated with a low resolution scaling cut-off at 18 Å . A weighting factor (w) was determined for each reflection to reduce the influence of outliers (Ren et al., 2001). From the weighted ΔF , a difference electron density map ($\Delta \rho$) is calculated using the program 'fft' from the ccp4 suite of programs (Winn et al., 2011). Since ΔF are on the absolute scale, $\Delta \rho$ is on half the absolute scale as a result of the difference Fourier approximation (Henderson and Moffat, 1971; Hondey et al., 2020).

Structure refinement of light structure

Extrapolated structural factors were assembled from amplitudes computed as $|F_e| = |F_c^{dark}| + \alpha * |\Delta F_o|$. The F_c^{dark} denotes the calculated structure factors of the refined dark structure ($DrBphP_{dark}$). The phases were taken from $DrBphP_{dark}$ is inversely related to the population of the photoinduced state by $(100/\alpha)*2$ ($Pandey\ et\ al.$, $Pandey\ et\ al.$). We estimated $Pandey\ et\ al.$ Dassed on $Pandey\ et\ al.$ Dassed

 F_e represents the pure structure factor of the photo-activated state (Figure 3—figure supplement 1). Refinement of a structural model was then performed in real and reciprocal space, using Coot (Emsley et al., 2010) and Phenix (Adams et al., 2010). The equilibrium values for the restraints used in the refinement of the biliverdin chromophore were taken from a minimal energy biliverdin ground state geometry that was obtained at the B3LYP/6-31G* level of density functional theory. Torsional restraints for the excited state geometry with the twisted D-ring were obtained at the SA (5)- CASSCF(12,12)/cc-pVDZ level of ab initio theory. We removed the torsion restrains for the C/Dring (C14-C15-C16-C17; C14-C15-C16-ND; C13-C14-C15-C16; NC-C14-C15-C16) and for the A/Bring (C3-C4-C5-C6; NA-C4-C5-C6; C4-C5-C6-C7; C4-C5-C6-NB) during refinement. The overall aim of the refinement was to maximize the agreement between the observed and calculated difference maps. To evaluate the agreement, we subtracted the calculated from the observed difference electron density $(\Delta \rho_o - \Delta \rho_c)$. The computation of this difference-difference maps require scaling of the maps to each other. To do so, the highest and lowest intensities of $\Delta \rho_o$ were scaled to the corresponding maximum and minimum of $\Delta \rho_c$ and the observed $\Delta \rho_o$ were interpolated linearly according to this scaling. The resulting difference-difference electron density map was used to identify sites, which required further optimization in subsequent refinement steps. Calculation of Pearson Correlation Coefficient (PCC) values between the $\Delta \rho_o$ and $\Delta \rho_c$ were applied to guide refinement of specific regions, such as the D-ring and the whole chromophore region. To do so, the correlation was determined based on electron density within a sphere with a radius of 3.5 Å or 10 Å centred on the D-ring or pyrrole water, respectively. As a final step in the refinement procedure, we refined the models with REFMAC version 5.8.0135 (Murshudov et al., 2011) with high geometry restraints (weight factor 0.005). This was done against phased extrapolated structure factors, using the phases of the refined light and dark structure for computation of phased ΔF as described (Pande et al., 2016). The structures did not change much, although the R factors dropped in this last step of refinement to Rwork/Rfree of 0.230/0.256 (Table 1). The coordinates and structure factors have been deposited in the Protein Data Bank under the accession code 6T3U.



Acknowledgements

The experiments at SACLA were performed at BL3 with the approval of the Japan Synchrotron Radiation Research Institute (JASRI) (Proposal No. 2018A8055 and 2019A8007). SW acknowledges the European Research Council for support (grant number: 279944). This work was supported by Academy of Finland grants 285461 and 296135 (HT and JAI, respectively) and Jane and Aatos Erkko foundation (JAI). This research is partially supported by Platform Project for Supporting Drug Discovery and Life Science Research (Basis for Supporting Innovative Drug Discovery and Life Science Research (BINDS)) from Japan Agency for Medical Research and Development (AMED). We thank Dr. Takanori Nakane for assistance with data processing during the beamtime and Heli Lehtivuori for the spectroscopic measurements with the microcrystals. This work was supported by NSF Science and Technology Centers grant NSF-1231306 ('Biology with X-ray Lasers') (MS), the National Science Foundation (NSF)-MCB-RUI 1413360 and NSF-MCB-EAGER 1839513 Research Grants to EAS. This work has been done as part of the BioExcel CoE (www.bioexcel.eu), a project funded by the European Union contracts H2020-INFRAEDI-02-2018-823830 and H2020-EINFRA-2015-1-675728 (GG).

Additional information

Funding

Funder	Grant reference number	Author
European Research Council	279944	Sebastian Westenhoff
Academy of Finland	285461	Heikki Takala
Academy of Finland	296135	Janne A Ihalainen
Jane and Aatos Erkko Foundation		Janne A Ihalainen
National Science Foundation	(NSF)-MCB-RUI 141336	Emina A Stojković
National Science Foundation	NSF-MCB-EAGER 183951	Emina A Stojković
Horizon 2020	H2020-INFRAEDI-02-2018- 82383	Gerrit Groenhof
Horizon 2020	H2020-EINFRA-2015-1- 67572	Gerrit Groenhof
National Science Foundation	NSF-1231306	Marius Schmidt

The funders had no role in study design, data collection and interpretation, or the decision to submit the work for publication.

Author contributions

Elin Claesson, Planned experiments, Purified the protein and prepared the microcrystals, Acquired the data at SACLA, Computed difference electron density maps and refined the structural models, Wrote the paper with input from all authors; Weixiao Yuan Wahlgren, Heikki Takala, Purified the protein and prepared the microcrystals, Acquired the data at SACLA, Computed difference electron density maps and refined the structural models; Suraj Pandey, Acquired the data at SACLA and processed the crystallography data; Leticia Castillon, Purified the protein and prepared the microcrystals, Acquired the data at SACLA; Valentyna Kuznetsova, Acquired the data at SACLA, Measured the UV-Vis spectroscopic data; Léocadie Henry, Matthijs Panman, Melissa Carrillo, Joachim Kübel, Rahul Nanekar, Linnéa Isaksson, Amke Nimmrich, Andrea Cellini, Michał Maj, Robert Bosman, Eriko Nango, Rie Tanaka, Tomoyuki Tanaka, Luo Fangjia, So Iwata, Shigeki Owada, Emina A Stojković, Acquired the data at SACLA; Dmitry Morozov, Gerrit Groenhof, Provided the geometry restrains biliverdin in the excited state; Moona Kurttila, Measured the UV-Vis spectroscopic data; Keith Moffat, Conceived the experiments; Janne A Ihalainen, Conceived the experiments, Acquired the data at SACLA; Marius Schmidt, Conceived the experiments, Acquired the data at SACLA, Computed difference electron density maps and refined the structural models, Wrote the paper with input from all authors; Sebastian Westenhoff, Conceived the experiments, Planned experiments, Acquired the



data at SACLA, Computed difference electron density maps and refined the structural models, Wrote the paper with input from all authors

Author ORCIDs

Weixiao Yuan Wahlgren (b) https://orcid.org/0000-0003-0413-165X Heikki Takala (b) https://orcid.org/0000-0003-2518-8583 Matthijs Panman (b) http://orcid.org/0000-0003-3853-123X Janne A Ihalainen (b) https://orcid.org/0000-0002-8741-1587 Sebastian Westenhoff (b) https://orcid.org/0000-0002-6961-8015

Decision letter and Author response

Decision letter https://doi.org/10.7554/eLife.53514.sa1 Author response https://doi.org/10.7554/eLife.53514.sa2

Additional files

Supplementary files

• Transparent reporting form

Data availability

Crystallography data have been submitted to protein data bank (PDB) dark:ID: D_1292104678 and PDB ID: 6T3L 1ps:ID: D_1292104679 and PDB ID: 6T3U. Raw diffraction images are deposited under ID 121 at CXIDB.

The following datasets were generated:

Author(s)	Year	Dataset title	Dataset URL	Database and Identifier
Claesson E, Wahlgren WY, Ta- kala H, Pandey S, Castillon L, Kuznet- sova V, Henry L, Panman M, Carrillo M, Kübel J, Nane- kar R, Isaksson L, Nimmrich A, Cellini A, Morozov D, Maj M, Kurttila M, Bosman R, Nango E, Tanaka R, Tana- ka T, Fangjia L, Iwata S, Owada S, Moffat K, Groenhof G, Stojković EA, Ihalainen JA, Schmidt M, Wes- tenhoff S	2020	The primary structural photoresponse of phytochrome proteins captured by a femtosecond X-ray laser	http://cxidb.org/id-121. html	CXIDB, 10.11577/160 7859
Claesson E, Takala H, Wahlgren W, Pandey S, Schmidt M, Westenhoff S	2020	PAS-GAF fragment from Deinococcus radiodurans phytochrome in dark state	http://www.rcsb.org/ structure/6T3L	RCSB Protein Data Bank, 6T3L
Claesson E, Takala H, Wahlgren W, Pandey S, Schmidt M, Westenhoff S	2020	PAS-GAF fragment from Deinococcus radiodurans phytochrome 1ps after photoexcitation	http://www.rcsb.org/ structure/6T3U	RCSB Protein Data Bank, 6T3U

References

Adams PD, Afonine PV, Bunkóczi G, Chen VB, Davis IW, Echols N, Headd JJ, Hung LW, Kapral GJ, Grosse-Kunstleve RW, McCoy AJ, Moriarty NW, Oeffner R, Read RJ, Richardson DC, Richardson JS, Terwilliger TC, Zwart PH. 2010. PHENIX: a comprehensive Python-based system for macromolecular structure solution. Acta



- Crystallographica Section D Biological Crystallography **66**:213–221. DOI: https://doi.org/10.1107/S0907444909052925, PMID: 20124702
- Barends TR, Foucar L, Ardevol A, Nass K, Aquila A, Botha S, Doak RB, Falahati K, Hartmann E, Hilpert M, Heinz M, Hoffmann MC, Köfinger J, Koglin JE, Kovacsova G, Liang M, Milathianaki D, Lemke HT, Reinstein J, Roome CM, et al. 2015. Direct observation of ultrafast collective motions in CO myoglobin upon ligand dissociation. Science 350:445–450. DOI: https://doi.org/10.1126/science.aac5492, PMID: 26359336
- Barty A, Kirian RA, Maia FR, Hantke M, Yoon CH, White TA, Chapman H. 2014. Cheetah: software for high-throughput reduction and analysis of serial femtosecond X-ray diffraction data. Journal of Applied Crystallography 47:1118–1131. DOI: https://doi.org/10.1107/S1600576714007626, PMID: 24904246
- Battye TG, Kontogiannis L, Johnson O, Powell HR, Leslie AG. 2011. iMOSFLM: a new graphical interface for diffraction-image processing with MOSFLM. Acta Crystallographica. Section D, Biological Crystallography 67: 271–281. DOI: https://doi.org/10.1107/S0907444910048675, PMID: 21460445
- Burgie ES, Wang T, Bussell AN, Walker JM, Li H, Vierstra RD. 2014. Crystallographic and electron microscopic analyses of a bacterial phytochrome reveal local and global rearrangements during photoconversion. *Journal of Biological Chemistry* 289:24573–24587. DOI: https://doi.org/10.1074/jbc.M114.571661, PMID: 25006244
- Burgie ES, Zhang J, Vierstra RD. 2016. Crystal structure of Deinococcus phytochrome in the photoactivated state reveals a cascade of structural rearrangements during photoconversion. Structure 24:448–457. DOI: https://doi. org/10.1016/j.str.2016.01.001, PMID: 26853942
- **Butler WL**, Norris KH, Siegelman HW, Hendricks SB. 1959. Detection, assay, and preliminary purification of the pigment controlling photoresponsive development of plants. *PNAS* **45**:1703–1708. DOI: https://doi.org/10. 1073/pnas.45.12.1703
- Coquelle N, Sliwa M, Woodhouse J, Schirò G, Adam V, Aquila A, Barends TRM, Boutet S, Byrdin M, Carbajo S, De la Mora E, Doak RB, Feliks M, Fieschi F, Foucar L, Guillon V, Hilpert M, Hunter MS, Jakobs S, Koglin JE, et al. 2018. Chromophore twisting in the excited state of a photoswitchable fluorescent protein captured by time-resolved serial femtosecond crystallography. *Nature Chemistry* 10:31–37. DOI: https://doi.org/10.1038/nchem.2853, PMID: 29256511
- Dasgupta J, Frontiera RR, Taylor KC, Lagarias JC, Mathies RA. 2009. Ultrafast excited-state isomerization in phytochrome revealed by femtosecond stimulated raman spectroscopy. PNAS 106:1784–1789. DOI: https://doi.org/10.1073/pnas.0812056106, PMID: 19179399
- Duisenberg AJM. 1992. Indexing in single-crystal diffractometry with an obstinate list of reflections. *Journal of Applied Crystallography* 25:92–96. DOI: https://doi.org/10.1107/S0021889891010634
- Edlund P, Takala H, Claesson E, Henry L, Dods R, Lehtivuori H, Panman M, Pande K, White T, Nakane T, Berntsson O, Gustavsson E, Båth P, Modi V, Roy-Chowdhury S, Zook J, Berntsen P, Pandey S, Poudyal I, Tenboer J, et al. 2016. The room temperature crystal structure of a bacterial phytochrome determined by serial femtosecond crystallography. *Scientific Reports* 6:35279. DOI: https://doi.org/10.1038/srep35279, PMID: 27756898
- Emsley P, Lohkamp B, Scott WG, Cowtan K. 2010. Features and development of coot. Acta Crystallographica. Section D, Biological Crystallography 66:486–501. DOI: https://doi.org/10.1107/S0907444910007493, PMID: 20383002
- Essen L-O, Mailliet J, Hughes J. 2008. The structure of a complete phytochrome sensory module in the pr ground state. PNAS 105:14709–14714. DOI: https://doi.org/10.1073/pnas.0806477105
- Gan F, Zhang S, Rockwell NC, Martin SS, Lagarias JC, Bryant DA. 2014. Extensive remodeling of a cyanobacterial photosynthetic apparatus in far-red light. *Science* **345**:1312–1317. DOI: https://doi.org/10.1126/science. 1256963, PMID: 25214622
- **Gustavsson E**, Isaksson L, Persson C, Mayzel M, Brath U, Vrhovac L, Ihalainen JA, Karlsson BG, Orekhov V, Westenhoff S. 2020. Modulation of structural heterogeneity controls phytochrome photoswitching. *Biophysical Journal* **118**:415–421. DOI: https://doi.org/10.1016/j.bpj.2019.11.025
- Henderson R, Moffat JK. 1971. The difference fourier technique in protein crystallography: errors and their treatment. Acta Crystallographica Section B Structural Crystallography and Crystal Chemistry 27:1414–1420. DOI: https://doi.org/10.1107/S0567740871004060
- Heyne K, Herbst J, Stehlik D, Esteban B, Lamparter T, Hughes J, Diller R. 2002. Ultrafast dynamics of phytochrome from the Cyanobacterium synechocystis, reconstituted with phycocyanobilin and phycoerythrobilin. *Biophysical Journal* 82:1004–1016. DOI: https://doi.org/10.1016/S0006-3495(02)75460-X, PMID: 11806940
- Ihalainen JA, Gustavsson E, Schroeder L, Donnini S, Lehtivuori H, Isaksson L, Thöing C, Modi V, Berntsson O, Stucki-Buchli B, Liukkonen A, Häkkänen H, Kalenius E, Westenhoff S, Kottke T. 2018. Chromophore-Protein interplay during the phytochrome photocycle revealed by Step-Scan FTIR spectroscopy. *Journal of the American Chemical Society* 140:12396–12404. DOI: https://doi.org/10.1021/jacs.8b04659, PMID: 30183281
- Lamparter T, Mittmann F, Gärtner W, Börner T, Hartmann E, Hughes J. 1997. Characterization of recombinant phytochrome from the Cyanobacterium synechocystis. PNAS 94:11792–11797. DOI: https://doi.org/10.1073/pnas.94.22.11792, PMID: 9342316
- Lehtivuori H, Rissanen I, Takala H, Bamford J, Tkachenko NV, Ihalainen JA. 2013. Fluorescence properties of the chromophore-binding domain of bacteriophytochrome from Deinococcus radiodurans. *The Journal of Physical Chemistry B* 117:11049–11057. DOI: https://doi.org/10.1021/jp312061b, PMID: 23464656
- Lim S, Yu Q, Gottlieb SM, Chang CW, Rockwell NC, Martin SS, Madsen D, Lagarias JC, Larsen DS, Ames JB. 2018. Correlating structural and photochemical heterogeneity in cyanobacteriochrome NpR6012g4. *PNAS* 115: 4387–4392. DOI: https://doi.org/10.1073/pnas.1720682115, PMID: 29632180



- McCoy AJ, Grosse-Kunstleve RW, Adams PD, Winn MD, Storoni LC, Read RJ. 2007. Phaser crystallographic software. *Journal of Applied Crystallography* **40**:658–674. DOI: https://doi.org/10.1107/S0021889807021206, PMID: 19461840
- Murshudov GN, Skubák P, Lebedev AA, Pannu NS, Steiner RA, Nicholls RA, Winn MD, Long F, Vagin AA. 2011. REFMAC5 for the refinement of macromolecular crystal structures. *Acta Crystallographica Section D Biological Crystallography* 67:355–367. DOI: https://doi.org/10.1107/S0907444911001314, PMID: 21460454
- Nakane T, Joti Y, Tono K, Yabashi M, Nango E, Iwata S, Ishitani R, Nureki O. 2016. Data processing pipeline for serial femtosecond crystallography at SACLA. *Journal of Applied Crystallography* 49:1035–1041. DOI: https://doi.org/10.1107/S1600576716005720, PMID: 27275146
- Nogly P, Weinert T, James D, Carbajo S, Ozerov D, Furrer A, Gashi D, Borin V, Skopintsev P, Jaeger K, Nass K, Båth P, Bosman R, Koglin J, Seaberg M, Lane T, Kekilli D, Brünle S, Tanaka T, Wu W, et al. 2018. "Retinal isomerization in bacteriorhodopsin captured by a femtosecond x-ray laser,". *Science* **361**:eaat0094. DOI: https://doi.org/10.1126/science.aat0094, PMID: 29903883
- Nosenko Y, Wiosna-Sałyga G, Kunitski M, Petkova I, Singh A, Buma WJ, Thummel RP, Brutschy B, Waluk J. 2008. Proton transfer with a twist? femtosecond dynamics of 7-(2-pyridyl)indole in condensed phase and in supersonic jets. *Angewandte Chemie International Edition* 47:6037–6040. DOI: https://doi.org/10.1002/anie. 200801350, PMID: 18604789
- Otero LH, Klinke S, Rinaldi J, Velázquez-Escobar F, Mroginski MA, Fernández López M, Malamud F, Vojnov AA, Hildebrandt P, Goldbaum FA, Bonomi HR. 2016. Structure of the Full-Length bacteriophytochrome from the plant pathogen Xanthomonas campestris provides clues to its Long-Range signaling mechanism. *Journal of Molecular Biology* 428:3702–3720. DOI: https://doi.org/10.1016/j.jmb.2016.04.012, PMID: 27107635
- Pande K, Hutchison CD, Groenhof G, Aquila A, Robinson JS, Tenboer J, Basu S, Boutet S, DePonte DP, Liang M, White TA, Zatsepin NA, Yefanov O, Morozov D, Oberthuer D, Gati C, Subramanian G, James D, Zhao Y, Koralek J, et al. 2016. Femtosecond structural dynamics drives the trans/cis isomerization in photoactive yellow protein. Science 352:725–729. DOI: https://doi.org/10.1126/science.aad5081, PMID: 27151871
- Pandey S, Bean R, Sato T, Poudyal I, Bielecki J, Cruz Villarreal J, Yefanov O, Mariani V, White TA, Kupitz C, Hunter M, Abdellatif MH, Bajt S, Bondar V, Echelmeier A, Doppler D, Emons M, Frank M, Fromme R, Gevorkov Y, et al. 2020. Time-resolved serial femtosecond crystallography at the european XFEL. *Nature Methods* 17:73–78. DOI: https://doi.org/10.1038/s41592-019-0628-z, PMID: 31740816
- Quail PH, Boylan MT, Parks BM, Short TW, Xu Y, Wagner D. 1995. Phytochromes: photosensory perception and signal transduction. Science 268:675–680. DOI: https://doi.org/10.1126/science.7732376, PMID: 7732376
- Ren Z, Perman B, Srajer V, Teng TY, Pradervand C, Bourgeois D, Schotte F, Ursby T, Kort R, Wulff M, Moffat K. 2001. A molecular movie at 1.8 A resolution displays the photocycle of photoactive yellow protein, a eubacterial blue-light receptor, from nanoseconds to seconds. *Biochemistry* 40::13788–13801. DOI: https://doi.org/10.1021/bi0107142, PMID: 11705368
- Rockwell NC, Shang L, Martin SS, Lagarias JC. 2009. Distinct classes of red/far-red photochemistry within the phytochrome superfamily. PNAS 106:6123–6127. DOI: https://doi.org/10.1073/pnas.0902370106, PMID: 1933 9496
- Rüdiger W, Thümmler F, Cmiel E, Schneider S. 1983. Chromophore structure of the physiologically active form (P (fr)) of phytochrome. PNAS 80:6244–6248. DOI: https://doi.org/10.1073/pnas.80.20.6244, PMID: 16593380
- Sanchez JC, Carrillo M, Pandey S, Noda M, Aldama L, Feliz D, Claesson E, Wahlgren WY, Tracy G, Duong P, Nugent AC, Field A, Šrajer V, Kupitz C, Iwata S, Nango E, Tanaka R, Tanaka T, Fangjia L, Tono K, et al. 2019. High-resolution crystal structures of a myxobacterial phytochrome at cryo and room temperatures. Structural Dynamics 6:054701. DOI: https://doi.org/10.1063/1.5120527, PMID: 31559319
- Schmidt A, Sauthof L, Szczepek M, Lopez MF, Escobar FV, Qureshi BM, Michael N, Buhrke D, Stevens T, Kwiatkowski D, von Stetten D, Mroginski MA, Krauß N, Lamparter T, Hildebrandt P, Scheerer P. 2018. Structural snapshot of a bacterial phytochrome in its functional intermediate state. *Nature Communications* 9: 4912. DOI: https://doi.org/10.1038/s41467-018-07392-7, PMID: 30464203
- Song C, Psakis G, Lang C, Mailliet J, Gartner W, Hughes J, Matysik J. 2011. Two ground state isoforms and a chromophore D-ring photoflip triggering extensive intramolecular changes in a canonical phytochrome. PNAS 108:3842–3847. DOI: https://doi.org/10.1073/pnas.1013377108
- Song C, Psakis G, Kopycki J, Lang C, Matysik J, Hughes J. 2014. The D-ring, not the A-ring, rotates in Synechococcus OS-B' Phytochrome. Journal of Biological Chemistry 289:2552–2562. DOI: https://doi.org/10. 1074/jbc.M113.520031
- Song C, Mroginski MA, Lang C, Kopycki J, Gärtner W, Matysik J, Hughes J. 2018. 3d structures of plant phytochrome A as pr and pfr from Solid-State NMR: implications for molecular function. *Frontiers in Plant Science* 9:1–15. DOI: https://doi.org/10.3389/fpls.2018.00498
- Stojković EA, Toh KC, Alexandre MT, Baclayon M, Moffat K, Kennis JT. 2014. FTIR spectroscopy revealing Light-Dependent refolding of the conserved tongue region of bacteriophytochrome. *The Journal of Physical Chemistry Letters* 5:2512–2515. DOI: https://doi.org/10.1021/jz501189t, PMID: 25126387
- Takala H, Björling A, Berntsson O, Lehtivuori H, Niebling S, Hoernke M, Kosheleva I, Henning R, Menzel A, Ihalainen JA, Westenhoff S. 2014. Signal amplification and transduction in phytochrome photosensors. *Nature* 509:245–248. DOI: https://doi.org/10.1038/nature13310, PMID: 24776794
- **Toh KC**, Stojkovic EA, van Stokkum IH, Moffat K, Kennis JT. 2010. Proton-transfer and hydrogen-bond interactions determine fluorescence quantum yield and photochemical efficiency of bacteriophytochrome. *PNAS* **107**:9170–9175. DOI: https://doi.org/10.1073/pnas.0911535107, PMID: 20435909



- Tono K, Nango E, Sugahara M, Song C, Park J, Tanaka T, Tanaka R, Joti Y, Kameshima T, Ono S, Hatsui T, Mizohata E, Suzuki M, Shimamura T, Tanaka Y, Iwata S, Yabashi M. 2015. Diverse application platform for hard X-ray diffraction in SACLA (DAPHNIS): application to serial protein crystallography using an X-ray free-electron laser. *Journal of Synchrotron Radiation* 22:532–537. DOI: https://doi.org/10.1107/S1600577515004464, PMID: 25931065
- van Thor JJ, Ronayne KL, Towrie M. 2007. Formation of the early photoproduct lumi-R of cyanobacterial phytochrome cph1 observed by ultrafast mid-infrared spectroscopy. *Journal of the American Chemical Society* 129:126–132. DOI: https://doi.org/10.1021/ja0660709, PMID: 17199291
- Wagner JR, Brunzelle JS, Forest KT, Vierstra RD. 2005. A light-sensing knot revealed by the structure of the chromophore-binding domain of phytochrome. *Nature* 438:325–331. DOI: https://doi.org/10.1038/ nature04118, PMID: 16292304
- Wagner JR, Zhang J, von Stetten D, Günther M, Murgida DH, Mroginski MA, Walker JM, Forest KT, Hildebrandt P, Vierstra RD. 2008. Mutational analysis of Deinococcus radiodurans bacteriophytochrome reveals key amino acids necessary for the photochromicity and proton exchange cycle of phytochromes. *Journal of Biological Chemistry* 283:12212–12226. DOI: https://doi.org/10.1074/jbc.M709355200, PMID: 18192276
- White TA, Kirian RA, Martin AV, Aquila A, Nass K, Barty A, Chapman HN. 2012. CrystFEL: a software suite for snapshot serial crystallography. Journal of Applied Crystallography 45:335–341. DOI: https://doi.org/10.1107/ S0021889812002312
- Winn MD, Ballard CC, Cowtan KD, Dodson EJ, Emsley P, Evans PR, Keegan RM, Krissinel EB, Leslie AG, McCoy A, McNicholas SJ, Murshudov GN, Pannu NS, Potterton EA, Powell HR, Read RJ, Vagin A, Wilson KS. 2011. Overview of the CCP4 suite and current developments. *Acta Crystallographica. Section D, Biological Crystallography* 67:235–242. DOI: https://doi.org/10.1107/S0907444910045749, PMID: 21460441
- Yang X, Kuk J, Moffat K. 2008. Crystal structure of *Pseudomonas aeruginosa* bacteriophytochrome: photoconversion and signal transduction. *PNAS* **105**:14715–14720. DOI: https://doi.org/10.1073/pnas. 0806718105, PMID: 18799746
- Yang X, Ren Z, Kuk J, Moffat K. 2011. Temperature-scan cryocrystallography reveals reaction intermediates in bacteriophytochrome. *Nature* 479:428–432. DOI: https://doi.org/10.1038/nature10506, PMID: 22002602
- Yang Y, Linke M, von Haimberger T, Hahn J, Matute R, González L, Schmieder P, Heyne K. 2012. Real-time tracking of phytochrome's orientational changes during Pr photoisomerization. *Journal of the American Chemical Society* 134:1408–1411. DOI: https://doi.org/10.1021/ja209413d, PMID: 22229806